PCCP

Accepted Manuscript

ROYAL SOCIETY OF CHEMISTRY

www.rsc.org/pccp

Journal Name

ARTICLE TYPE

Cite this: DOI: 10.1039/xxxxxxxxxx

Intermediate photofragment distributions as probes of non-adiabatic dynamics at conical intersections: Application to the Hartley band of ozone†

David Picconi[a] and Sergy Yu. Grebenshchikov[a]*

Received Date
Accepted Date

DOI: 10.1039/xxxxxxxxxx

www.rsc.org/journalname

Quantum dynamics at a reactive two-state conical intersection lying outside the Franck-Condon zone is studied for a prototypical reaction of ultraviolet photodissociation of ozone in the Hartley band. The focus is on the vibrational distributions in the two electronic states at intermediate interfragment distances near the intersection. Such intermediate distributions of strongly interacting photofragments contain unique information on the location and shape of the conical intersection. Multidimensional Landau-Zener modeling provides a framework to reverse engineer the molecular geometry-dependent Massey parameter of the intersection from the intermediate distributions. The conceptual approach is demonstrated for the intermediate O−O bond stretch distributions which become strongly inverted on adiabatic passage through the intersection. It is further demonstrated that intermediate distributions can be reconstructed from the photoemission spectrum of the dissociating molecule. The illustration, given using quantum mechanical calculations of resonance Raman profiles for ozone, completes a practicable cycle of conversion of intermediate distributions into topographic features of the conical intersection.

1 Introduction

Conical intersections of electronic states are a focus of extensive experimental and theoretical scrutiny in the domain of reaction dynamics: The presently accumulated evidence indicates that conical intersections are common in the excited electronic states and therefore are likely to be encountered as the excited molecule moves along the reaction coordinate.[1] Such *reactive* conical intersections are postulated to mediate ultrafast (femtosecond-scale) radiationless transitions and are recognized as natural molecular hubs, or generalized transition states, routing the reactive system towards specific final states or specific products.[2,3] The knowledge of their energetic position and topography is often regarded as instrumental to the ability to control elementary reactive steps in, for example, organic photochemistry, photobiology, or molecular electronics.[1,3] At a more fundamental level, reactive conical intersections represent molecular sites at which the characteristic time scales of electronic and nuclear motions become compatible, and the correlated electron-nuclear dynamics can be effectively probed.[4,5] This paper demonstrates how to locate reactive conical intersections and to characterize their shape using excitation distributions in the modes transverse to the reaction path.

Recent years have seen a growing effort to detect reactive conical intersections experimentally.[6,7] For a molecule with N_c nuclear degrees of freedom, a conical intersection is characterized (a) by an (N_c-2) dimensional space of coordinates $\{Z\}$, called *seam space*, in which the energies of the intersecting states stay equal, and (b) by a two dimensional *branching space* (X,Y), in which the degeneracy is lifted. The familiar hourglass picture of a conical intersection, with 'sand' (i.e. the state population) flowing from the upper into the lower cone, refers to the branching space: The reaction complex switches electronic states only if it moves in the coordinates (X,Y). This suggests that experimentally conspicuous reactive conical intersections arise if the reaction path lies in their branching space.[8]

The non-adiabatic molecular photodissociation provides an effective means to probe reactive conical intersections with a fully controlled initial state.[1,7,9,10] A prototypical arrangement of electronic states is illustrated in Fig. 1(a) in a potential energy diagram. The photoexcitation from the ground electronic state $\tilde{X}$ brings the molecule into a single optically bright diabatic electronic state B shown with blue. The B state forms an intersection (marked with a circle) with another diabatic electronic state R shown in red. The coordinate X in this diagram is the *tuning mode* of the intersection: The energy difference between the B and R states along X changes the fastest. The second coordinate of the branching space, Y, is perpendicular to the plane of the fig-

[a] Department of Chemistry, Technische Universität München, Lichtenbergstr. 4, 85747 Garching, Germany
* E-mail: Sergy.Grebenshchikov@ch.tum.de

† Electronic Supplementary Information (ESI) available. See DOI: 10.1039/b000000x/

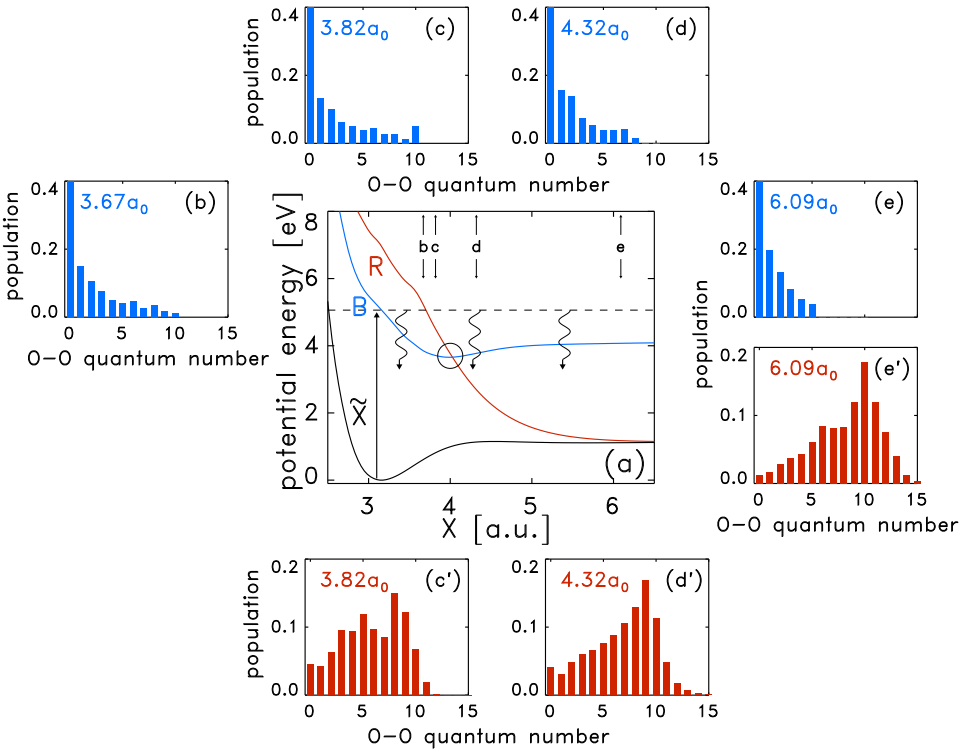

Fig. 1 (a) A one dimensional cut along the interfragment Jacobi distance X through the ab initio potential energy surfaces of the electronic states $\tilde{X}\,^1A'$ (black; marked $\tilde{X}$), $3\,^1A'$ (blue; marked B), and $^1A'$ (red; marked R), participating in the UV photodissociation of ozone. Two other Jacobi coordinates are optimized to give the minimum energy of the B state. The B/R conical intersection is marked with a circle. Straight line arrows indicate the distances $X_\star$, at which the distributions in panels (b−e) and (c′ −e′) are evaluated. Curved arrows represent emission of the dissociating molecule. (b−e) The normalized vibrational distributions in the short O−O bond stretch in the B state at fixed distances $X_\star$ indicated in each frame. (c′−e′) The same distributions, as in (c−e), but for the R state. The photon energy is $E_{\rm ph} = 4.96\,$eV (the photolysis wavelength $\lambda = 250\,$nm).

ure — it is the *coupling mode* along which the interstate coupling grows the fastest. The conical intersection is shifted halfway into the exit channel, and two distinct electronic dissociation channels emerge from the intersection. The dissociation coordinate in this example coincides with the tuning mode X. The state intersection pattern in Fig. 1(a) is characteristic of several broad classes of UV photodissociation reactions in which two fragments, an atom and a molecule, are formed. Examples of such *exit channel* intersections are found in the photodissociation of triatomic atmospheric trace gases (such as N_2O,[11] CO_2,[12,13] or O_3[14,15]), photodissociation of halogenoalkanes (in particular, methyl halides[16–19] CY_3I or CY_3Br, with Y = H, D, or F), and the currently much studied ultrafast decomposition of heteroaromatic molecules (such as pyrrole[9] or phenol and its derivatives[7,20,21]) into an H atom and a radical co-fragment. Although the exit channel conical intersections lie outside the Franck-Condon zone and are difficult to detect spectroscopically, they influence the separating photofragments. Clearly affected are the observables associated with the tuning mode X, e.g. the electronic branching ratios and the total kinetic energy release, but those associated with the coupling mode Y (for example, rovibrational or angular distributions) are influenced, too. The information content of the distributions associated with the branching space (X,Y) can be illustrated using a Landau-Zener-type estimate.[15,22,23] The probability of a transition between the diabatic states B and R depends on the average[24] adiabatic energy gap $\overline{\Delta E}^{\rm ad}$ and the average sojourn time $\overline{\tau}_x$ in the crossing region, $w^{\rm LZ}(B \to R) \approx 1 - \exp(-\overline{\Delta E}^{\rm ad}\overline{\tau}_x)$. The more adiabatic the motion along X, the larger the gap between the adiabatic states, the longer the time spent near intersection, and the larger the transition probability $w^{\rm LZ}(B \to R)$. Molecules in the B state with no excitation in the coupling mode Y are moving fast through the region of small gap $\overline{\Delta E}^{\rm ad}$; as a result they behave diabatically and end up in the upper dissociation channel B. Molecules, moving in the B state with the mode Y strongly excited, sample large gaps $\overline{\Delta E}^{\rm ad}$ and move slowly along X; as a result they are diverted into the lower dissociation channel R. The conical intersection acts as a 'beam splitter', sending the X-slow/Y-excited fragments into one (adiabatic) channel and the X-fast/Y-cold fragments into the other (diabatic) channel. The final photofragment distributions in the adiabatic and the diabatic channels, if simultaneously observed, reveal the presence of the reactive conical intersection.[7,15,25] The major obstacle, however, are the post-intersection dynamics which are different in the two electronic channels and which distort the distributions arriving in the asymptotic region. The situation is somewhat similar to the one encountered in direct probing of a fleeting transition state in bimolecular reactions.[26] In the potential diagram in Fig. 1(a), an important source of such distortions is a nearly 3 eV difference in

the dissociation energies of the two channels.

This work shows that *intermediate* distributions, recorded in the vicinity of the intersection, carry structural and dynamical information about the shape of the conical intersection in the branching space. Our aim is to demonstrate how this information can be extracted from the vibrational distributions in the coupling mode Y, taken as the main example, and how the intermediate vibrational distributions themselves can be reconstructed from the emission spectrum of the dissociating molecule.

The ultraviolet (UV) photodissociation of ozone in the Hartley band serves as proof-of-principle application; this reaction is the key step in the protective function of the stratospheric ozone layer and the primary source of $O(^1D)$ oxygen in the atmosphere of Earth.[14,15,27–31] The diagram in Fig. 1(a) depicts three singlet electronic states involved in the reaction:[14,28,31] The ground electronic state $\tilde{X}\,^1A'$, the optically bright state $3\,^1A'$ ('B'), and the purely repulsive dark singlet state $^1A'$ ('R'). The two dissociation channels are spin-allowed and, combined, carry most of the reaction flux:[27,29]

$$E_{\rm ph.} > 1.051\,{\rm eV}:\ {\rm O_3}+\hbar\omega \quad \rightarrow \quad {\rm O}(^3{\rm P})+{\rm O_2}(X\,^3\Sigma_g^-) \qquad (1)$$

$$E_{\rm ph.} > 4.000\,{\rm eV}:\ {\rm O_3}+\hbar\omega \quad \rightarrow \quad {\rm O}(^1{\rm D})+{\rm O_2}(a\,^1\Delta_g)\,. \qquad (2)$$

In the 'singlet' channel (2), reached diabatically along the B state, O and O_2 are electronically excited; this is the major reaction channel accounting for $\sim 90\%$ of the products. In the 'triplet' channel (1), reached adiabatically by taking a hop to the R state, the fragments are formed in their ground electronic states; this is a minor channel with the quantum yield between 7% and 9%. Molecules, photoexcited into the B state, branch between the two channels at the B/R conical intersection. The tuning mode X is the $O\cdots O_2$ distance; the coupling mode Y is the short (fragment) O−O bond length. Photodissociation in the Hartley band has been exhaustively described using quantum mechanics.[15] The calculations with the ab initio potentials of Ref. 31, accurately reproduce the temperature dependent[32] Hartley absorption spectrum with its weak diffuse bands and the final rovibrational and angular photofragment distributions.

The diffuse absorption spectrum reflects early photodissociation dynamics in the Franck-Condon region; the asymptotic distributions are shaped by the integrated effect of all interactions acting along the dissociation path. In this work, we concentrate on intermediate dissociation distances near the conical intersection, and use quantum mechanical calculations to construct vibronic distributions of the emerging but still interacting photofragments over the local vibrational modes transverse to the dissociation path. The approach to calculation of intermediate distributions is described in Sect. 2. In Sect. 3, the intermediate distributions are used to track the non-adiabatic dynamics at the conical intersection with spatial and energy resolution, and to visualize the bond breaking and energy redistribution in the photoexcited ozone. This analysis reveals an unexpectedly active energy exchange in the branching space, with up to 6 vibrational quanta (corresponding to the vibrational energy of more than 1.0 eV) transferred to the coupling mode upon crossing the intersection. The modelling of the intermediate distributions in the framework of Landau-Zener theory in Sect. 4 allows one to reverse engineer the parameters of the conical intersection. Finally, the intermediate distributions are inferred from the amplitudes of fluorescence into the ground electronic state in Sect. 5. Summary is given in Sect. 6. Technical information and numerical details are summarized in two Appendices and in the ESI.†

2 Vibronic distributions of interacting photofragments at intermediate interfragment distances

We shall consider the dissociation dynamics of the photoexcited ozone using the molecular Hamiltonian set in the quasi-diabatic representation:[33]

$$\hat{\mathbf{H}}^0 = \begin{pmatrix} \hat{T} & 0 \\ 0 & \hat{T} \end{pmatrix} + \begin{pmatrix} V_B & V_{BR} \\ V_{BR} & V_R \end{pmatrix}. \qquad (3)$$

$\hat{T}$ is the standard[34] kinetic energy operator for a non-rotating triatomic molecule, common for both electronic states and specified in the body fixed (BF) frame using the Jacobi coordinates $\mathbf{Q}=(X,Y,Z)$. The coordinate X (the tuning mode) is the distance between one oxygen atom and the center of mass of O_2, Y is the O−O distance (the coupling mode), and Z is the angle between the vectors $\mathbf{X}$ and $\mathbf{Y}$.

Internal electronic ($\gamma =$ B or R), vibrational (V) and rotational (J) states of the oxygen molecule label the asymptotic scattering channels (γ,J,V) whose populations give the asymptotic photofragment distributions $P_\gamma(J,V)$, defined in terms of the total and partial absorption cross sections. Meaningful and eventually observable vibronic distributions at intermediate interfragment separations $X_\star$ are constructed by smoothly continuing the channels (γ,J,V) into the inner region.

The photon energy dependent *total absorption cross section* is given by a Fourier transform of the autocorrelation function ($\hbar=1$ hereafter),

$$\sigma_{\rm tot}(E_{\rm ph}) = \frac{\pi E_{\rm ph}}{3c\varepsilon_0}\int_0^\infty \left\langle \Phi_0 \left| e^{-i\hat{\mathbf{H}}^0 t} \right| \Phi_0 \right\rangle e^{iE_{\rm ph}t}\,dt\ . \qquad (4)$$

The total cross section can be written in the equivalent form

$$\sigma_{\rm tot}(E_{\rm ph}) = \frac{E_{\rm ph}}{3c\varepsilon_0}\lim_{\lambda\to 0}\lambda\left\langle \mathbf{\Psi}^\lambda(\mathbf{Q}|E_{\rm ph})|\mathbf{\Psi}^\lambda(\mathbf{Q}|E_{\rm ph})\right\rangle\ , \qquad (5)$$

which involves the stationary energy component of the wave packet in two electronic states,

$$\mathbf{\Psi}^\lambda(\mathbf{Q}|E_{\rm ph}) = \int_0^\infty e^{-i(\mathbf{H}^0-i\lambda)t}\Phi_0 e^{-iE_{\rm ph}t}\,dt\ . \qquad (6)$$

The electronic components Ψ^λ_γ of the vector $\mathbf{\Psi}^\lambda$ contain purely outgoing waves along X. In practice, the infinitesimal damping λ, ensuring this asymptotic behaviour, enters the calculations as an absorbing potential described in Sect. I of the ESI.†

Using the completeness relation for the energy-normalized scattering eigenstates $\left\{\psi^-_{\gamma JV}\right\}$, the total cross section can be writ-

ten as a sum of *partial cross sections*,

$$\sigma_{\rm tot}(E_{\rm ph}) = \sum_{\gamma JV} \sigma_{\rm par}(E_{\rm ph}|\gamma JV) \ , \tag{7}$$

$$\sigma_{\rm par}(E_{\rm ph}|\gamma JV) = \frac{E_{\rm ph}}{3c\varepsilon_0} \lim_{\lambda\to 0} \lambda \left| \left\langle \psi^-_{\gamma JV} | \Psi^\lambda_\gamma(\mathbf{Q}|E_{\rm ph}) \right\rangle \right|^2 = \frac{E_{\rm ph}}{3c\varepsilon_0} |T_{\gamma JV}(E_{\rm ph})|^2 \ , \tag{8}$$

with the photodissociation matrix element – the central piece of the theory – given by

$$T_{\gamma JV}(E_{\rm ph}) = \lim_{\lambda\to 0} \lambda \left\langle \psi^-_{\gamma JV} | \Psi^\lambda_\gamma \right\rangle \ . \tag{9}$$

The normalized photofragment distributions $P_\gamma(J,V)$

$$P_\gamma(J,V) = \frac{1}{\mathcal{N}} \left| T_{\gamma JV}(E_{\rm ph}) \right|^2 , \tag{10}$$

are proportional to the squares of the T-matrix elements. The goal is to find a reliable continuation of the T-matrix elements to intermediate interfragment distances. Our approach extends the projection method of Balint-Kurti and coworkers,[35,36] originally developed for large intefragment distances and based on the asymptotic factorization of the wave function $\mathbf{\Psi}^\lambda(X;Y,Z|E_{\rm ph})$ into the X- and the (Y,Z)-dependent part in each dissociation channel,

$$\begin{aligned} \Psi^\lambda_\gamma(X;Y,Z|E_{\rm ph}) \xrightarrow{X\to\infty} \quad & -i\textstyle\sum_{JV} T_{\gamma JV}(E_{\rm ph}) \sqrt{\frac{\mu_X}{k_{\gamma JV}}} e^{ik_{\gamma JV}X} \chi_{\gamma JV}(Y,Z) \\ & \equiv \textstyle\sum_{JV} f_{\gamma JV}(X) \chi_{\gamma JV}(Y,Z) \ , \end{aligned} \tag{11}$$

where μ_X is the O/O_2 reduced mass, $\chi_{\gamma JV}(Y,Z)$ is the eigenfunction of the fragment state (γ,J,V), $\varepsilon_{\gamma JV}$ is its eigenenergy, and $k_{\gamma JV} = \sqrt{2\mu_X(E_{\rm ph}-\varepsilon_{\gamma JV})}$ is the channel momentum (atomic units $\hbar = 1$ are used).

In the asymptotic region, at the *analysis line* $X = X_\infty$, the fragment eigenstates form an orthogonal set, and the T-matrix element can be projected out of Eq. (11):

$$|T_{\gamma JV}(X_\infty)|^2 = \frac{k_{\gamma JV}}{\mu_X} \left| \langle \chi_{\gamma JV}(Y,Z) | \delta(X-X_\infty) | \Psi^\lambda_\gamma(X;Y,Z) \rangle \right|^2 \ . \tag{12}$$

In terms of the velocity operator $\hat{v}_X = \hat{p_X}/\mu_X$ and its real eigenvalues $\dot{X}_{\gamma JV} = k_{\gamma JV}/\mu_X$, Eq. (12) can be re-written as

$$|T_{\gamma JV}(X_\infty)|^2 = f^*_{\gamma JV}(X_\infty) \dot{X}_{\gamma JV} f_{\gamma JV}(X_\infty) \ . \tag{13}$$

An alternative formulation for the T-matrix element, developed by Manolopolous, Rist and Alexander[37,38] in the context of time-independent close coupling method and adapted by Zhang[34] for wave packet propagation, is based directly on the flux operator,

$$|T_{\gamma JV}(X_\infty)|^2 = {\rm Re}\left[f^*_{\gamma JV}(X_\infty) \hat{v}_X f_{\gamma JV}(X_\infty) \right] \ . \tag{14}$$

The Eqs. (13) and (14) are equivalent in the asymptotic region. Either of them can be used to continue of the T-matrix elements to arbitrary interfragment distances, $X_\star < X_\infty$, and to define the intermediate populations $P_\gamma(j,v)$. The corresponding continued channels (γ,j,v) are denoted with lowercase letters, with j standing for the local $\widehat{\rm OOO}$ bending and v for the short O–O bond stretching quantum numbers; the corresponding local eigenstates $\chi_{\gamma jv}(Y,Z|X_\star)$ have eigenenergies $\varepsilon_{\gamma jv}(X_\star)$. The wave functions $\chi_{\gamma jv}$ are calculated at a fixed intermediate distance $X_\star$ in the plane (Y,Z) transverse to the reaction path, and the wave function $\mathbf{\Psi}^\lambda$ is expanded in terms of the complete set of these eigenstates:

$$\Psi^\lambda_\gamma(\mathbf{Q}|E_{\rm ph}) = \sum_{jv} f_{\gamma jv}(X-X_\star) \chi_{\gamma jv}(Y,Z|X_\star) \ . \tag{15}$$

The functions $\{\chi_{\gamma jv}(Y,Z|X_\star)\}$ are the local transverse eigenstates, adiabatic in the vibrational and diabatic in the electronic degrees of freedom,[38] evaluated as eigenstates of the intermediate Hamiltonian with a fixed value of $X = X_\star$. In the limit $X_\star \to \infty$ they converge to the eigenstates of the free O_2.

The functions $f_{\gamma jv}(X-X_\star)$ describe the relative motion of the fragments along the reaction coordinate near $X_\star$ with the velocity $\dot{X}_{\gamma jv}$. They can be used to construct the intermediate T-matrix elements either via the expression

$$|T_{\gamma jv}(X_\star)|^2 = f^*_{\gamma jv}(0) \dot{X}_{\gamma jv} f_{\gamma jv}(0) \ , \tag{16}$$

which is analogous to Eq. (13), or via

$$|T_{\gamma jv}(X_\star)|^2 = {\rm Re}\left[f^*_{\gamma jv}(0) \hat{v}_X f_{\gamma jv}(0) \right] \ , \tag{17}$$

which is analogous to Eq. (14).

This gives the total cross section as a sum of partial components proportional to $\left|T_{\gamma jv}(X_\star)\right|^2$ and thus defines local vibrational populations in the transverse vibrationally adiabatic modes. The absolute squares of the T-matrix elements sum up to the same total absorption cross section for any $X_\star$. Alexander and co-workers used the Eq. (17) to define local reactive fluxes.[37,38] Intermediate distributions in this work are calculated using the Eq. (16). In principle, the two definitions lead to different results, because the functions $f_{\gamma jv}(X-X_\star)$ contain both incoming and outgoing waves and are no longer eigenfunctions of $\hat{v}_X$. Equation (17) is more physically sound: Due to flux conservation the reactive flux can be evaluated across arbitrary (closed) surface. On the other hand, the less rigorous Eq. (16) is easier to implement within an iterative propagation scheme, because it amounts to calculating only the projection integral

$$\left\langle \chi_{\gamma jv}(Y,Z|X_\star) \delta(X-X_\star) | \Psi^\lambda_\gamma(X;Y,Z|E_{\rm ph}) \right\rangle$$

at the *analysis line* $X = X_\star$. The calculation with Eq. (17) involves taking the derivative of this integral with respect to X. The distributions obtained using the two expressions are compared in Fig. S3 of the ESI;† they turn out to be nearly indistinguishable. The definition of Eq. (16) is also used in Sect. 5 to relate the T-matrix elements to resonance Raman amplitudes.

In practice, the normalized intermediate distributions in the electronic state γ,

$$P_\gamma(j,v) = \frac{1}{\mathcal{N}} \left| T_{\gamma jv}(E_{\rm ph}|X_\star) \right|^2 \tag{18}$$

are calculated by overlapping the evolving wave packet with the local projection eigenstates $\chi_{\gamma jv}$. The photodissociation matrix elements $T_{\gamma jv}$ are calculated as half-Fourier transforms of the overlaps $C_{\gamma jv}(t|X_\star)$ of the wave packet $\Phi_\gamma(t)$ with the local projection

states $\chi_{\gamma jv}(Y,Z|X_\star)$ at the analysis line $X_\star$:

$$C_{\gamma jv}(t|X_\star) = \left[\chi_{\gamma jv}|\Phi_\gamma(t)\right]_{X_\star} \quad (19)$$

$$\left|T_{\gamma jv}(E_{\rm ph}|X_\star)\right|^2 = \frac{k_{\gamma jv}(X_\star)}{\mu_X}\left|\int_0^\infty C_{\gamma jv}(t|X_\star)\exp(iE_{\rm ph}t)\,dt\right|^2 .$$

Here $k_{\gamma jv}(X_\star)=\sqrt{2\mu_X\left(E_{\rm ph}-\varepsilon_{\gamma jv}(X_\star)\right)}$ is the local channel momentum. Integration in square brackets $[\cdot|\cdot]_{X_\star}$ is carried out only over the coordinates (Y,Z) at $X=X_\star$.

3 Intermediate distributions in photodissociating ozone

Calculations on ozone are performed with the initial state

$$\Phi_0(\mathbf{Q}) = |\mu(\mathbf{Q})|\Psi_X(\mathbf{Q}), \quad (20)$$

which is the wave function of the ground vibrational state of non-rotating ozone in the ground electronic state $\tilde{X}$, multiplied by the transition dipole moment (TDM) between the states B and $\tilde{X}$. Such initial state, violating the optical selection rules and corresponding to a $J_i=0\to J_f=0$ transition, is often used in calculations of absorption spectra and partial cross sections, and it is demonstrated in Ref. 15 that this choice does not affect the product states distributions. In the photon energy range studied in this work, 4.5 eV $< E_{\rm ph} <$ 5.5 eV, only the B state can be initially populated (the vertical excitation energy to the R state is $\approx$ 9 eV). The *ab initio* coordinate dependent TDM components are taken from Ref. 39.

The intermediate distributions discussed below are calculated in two steps. First the non-stationary initial state of ozone in the optically bright B state is prepared according to Eq. (20). Next, this initial excitation in B is propagated under the influence of the molecular Hamiltonian of Eq. (3) describing the motion in the coupled ab initio potential energy surfaces B and R. Computational details are given in Sect. I of the ESI.†

The absolute squares of the T-matrix elements are calculated before and after the conical intersection (see Fig. 1), in the dynamically relevant region in which most of the population transfer from B to R takes place (see Sect. III of the ESI† for a definition of the intersection region and, in particular, Figs. S1 and S2 showing the intersection topography including the minimum energy intersection).

Vibrational distributions in the short O−O bond stretch describe the energy content of the coupling mode Y and their variation across the B/R intersection is remarkably different in the two electronic states. This is illustrated in panels (b)−(e) and (c′)−(e′) of Fig. 1. The panel (b) shows the local vibrational distribution $P_B(v)$ in the B state at $X_\star = 3.67\,a_0$, i.e. to the left of the intersection region: The molecule is in the B state, the R state is unpopulated. This intermediate distribution is the 'initial condition' for the coupled state dynamics at the conical intersection. It peaks at $v=0$ and rapidly falls off with growing v: Molecules in the B state arrive at the intersection region with only modestly excited short O−O bond. This incident distribution is preserved as ozone moves along the diabatic path across the intersection region [panels (c), (d), and (e)]. The only noticeable change with growing O···O_2 separation is a slight cooling off of the high-v tail adjusting itself to the rising potential energy of the fragments climbing towards the asymptotic singlet channel.

The shape of the incident distribution changes dramatically along the adiabatic path (c′)−(d′)−(e′) across the intersection. Only molecules with substantial excitation in the short O−O bond, sieved out of the tail of the incident distribution, emerge in the R state, and the vibrational distribution inverts in the intersection region and peaks at $v\approx 6-8$. The distance $X_\star \approx 4.0\,a_0$, at which the distribution becomes detectable (e.g., via emission to the ground electronic state, see Sect. 5), approximately marks the location of the conical intersection. The post-intersection R state dynamics broaden this distribution and shift its maximum to higher v values. The mismatch in the local equilibria of the O_2 moieties in B and R states is negligible and cannot explain the difference in the distributions.

The strongly inverted asymptotic vibrational distributions in the triplet channel (1), exemplified in panel (e′), have been measured in Ref. 40 (a detailed comparison between calculated and measured asymptotic vibrational distributions can be found in Fig. 5 of Ref. 15). The above analysis demonstrates that they are formed in the immediate vicinity of the conical intersection. Physically, the distributions are inverted because only the molecules with an over-stretched O—O bond emerge in the R state, following an adiabatic passage through the intersection. R state components of the stationary scattering wave functions, filtered out of the wave packet at fixed photon energies,[15] are peaked close to $Y\approx 2.9\,a_0$, which is $0.6\,a_0$ longer than the equilibrium O−O bond length in molecular oxygen.

4 Landau-Zener modelling and reverse engineering of the parameters of a conical intersection

The presented picture is qualitatively consistent with the Landau-Zener estimation: Molecules with a strongly excited high frequency O−O vibration lack translational energy in the tuning O···O_2 mode, spend long time in the intersection region, and make a transition from B to R state with large probability. This has previously been noticed in the Landau-Zener-based surface hopping trajectory calculations performed in Refs. 14,23,31. The efficiency with which the O_2 bond is excited is astonishing: The intermediate distributions in panels (b) and (c′) reveal that 6–8 vibrational quanta are transferred to the tuning mode on the adiabatic path, and more than 1.0 eV of vibrational energy is relocated over an interfragment displacement of $\sim 0.5\ a_0$. This energy has to be compared with the transfer of a single vibrational quantum (~ 0.17 eV), commonly expected in models based on the popular linear vibronic coupling Hamiltonian.[41] The origin of the active energy redistribution in the branching space is a strong superlinear dependence of the ab initio diabatic coupling element V_{BR} on the O−O bond distance. In a separate numerical experiment, the upper adiabatic surface has been removed from the calculation (see Appendix A). The resulting asymptotic O−O distributions in the R-channel differ drastically from the above two-state case:

They are cold and peak sharply at $v = 0$.

The Landau-Zener approach can also serve as a basis for quantitative modelling of the direct dissociation through an exit channel conical intersection.[16,43–45] Suppose that the system moves in the vicinity of the intersection along a straight line trajectory $X(t) = X_\star + \dot{X}_{jv}(t - t_\star)$ in the B state, and the coupling mode Y and the seam mode Z are in a local quantum state χ_{Bjv}; the velocity along the tuning mode is $\dot{X}_{jv} = \left\{2\left(E_{\rm ph} - \varepsilon_{Bjv}(X_\star)\right)/\mu_X\right\}^{1/2}$. The average[24,46] transition probability $w^{\rm LZ}_{jv}(B \to R)$ between the diabatic states B and R can be expressed in terms of the local Massey parameter $\xi_{jv}(X_\star)$,

$$w^{\rm LZ}_{jv}(B \to R) = 1 - \exp\left(-\xi_{jv}\right) \qquad (21)$$

$$\xi_{jv}(X_\star) = \frac{2\pi\left(V^2_{BR}\right)_{jv}}{\dot{X}_{jv}\left(\Delta F\right)_{jv}} .$$

$\xi_{jv}(X_\star)$ characterizes the local shape of the intersecting states, probed in the transverse quantum state χ_{Bjv}, in terms of the two key parameters, namely the expectation values of the diabatic coupling, $\left(V^2_{AB}\right)_{jv} = \left[\chi_{Bjv}|V^2_{AB}|\chi_{Bjv}\right]_{X_\star}$, and the difference of slopes of the diabatic potentials along X, $\left(\Delta F\right)_{jv} = \left[\chi_{Bjv}|\Delta F|\chi_{Bjv}\right]_{X_\star}$. Small $\xi_{jv} \to 0$ implies small transition probability $w^{\rm LZ}_{jv}(B \to R)$; dissociating molecules tend to stay in the diabatic B state as they pass through the conical intersection. Large ξ_{jv} corresponds to larger $w^{\rm LZ}_{jv}(B \to R)$, with more molecules diverted into the R state and dissociating adiabatically.

Estimates, based on the 'diagonal' (in j and v) state-averaged Landau-Zener model of Eq. (21), are remarkably accurate for ozone. For example, the population of the R state, evaluated near the conical intersection at $X_\star = 3.9\,a_0$ as a sum of all Landau-Zener transition probabilities $\sum_{jv} 1 - \exp\left(-\xi_{jv}\right)$, amounts to 0.040; the quantum mechanical value is 0.035 (the cited yields are for $E_{\rm ph} = 4.96$ eV). Another example is provided by the inverted vibrational distributions in the local O−O vibration in the R state. Their Landau-Zener counterparts are given by a convolution of the transition probability with the incident distribution $P_B(j,v)$ in the B state:

$$P^{\rm LZ}_R(v) = \sum_j w^{\rm LZ}_{jv}(B \to R) P_B(j,v) . \qquad (22)$$

The v dependence of $P_B(j,v)$ is shown in panel (a) of Fig. 2, and the Landau-Zener approximation $P^{\rm LZ}_R(v)$ is compared with the quantum intermediate distribution at $X_\star = 3.9\,a_0$ in panel (b). The agreement is good for $v \le 13$; higher vibrational quantum

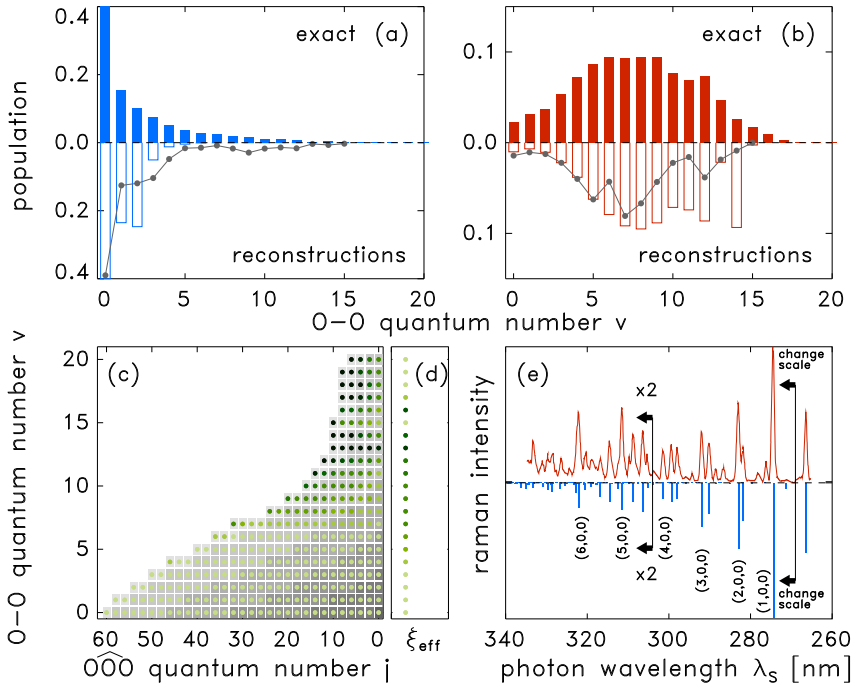

Fig. 2 (a) The normalized quantum vibrational distribution in the short O−O bond stretch in the B state evaluated at $X_\star = 3.90\,a_0$ (filled histograms). The same distribution reconstructed from the emission amplitudes α^B_{k0} into the bound states of $\tilde{X}$ is shown with empty histograms. Gray line depicts the reconstruction including emission into both bound and continuum states of $\tilde{X}$. (b) The normalized quantum vibrational distribution in the short O−O bond stretch in the R state evaluated at $X_\star = 3.90\,a_0$ (filled histograms). The same distribution reconstructed using the Landau-Zener equation (22) is shown with empty histograms. Gray line depicts the reconstruction based on the emission amplitudes α^R_{k0} into both bound and continuum states of $\tilde{X}$. (c) Two dimensional map of the Massey parameter $\xi_{jv}(X_\star)$ at $X_\star = 3.9\,a_0$ in the plane of the local quantum numbers v and j; light green color corresponds to $\xi_{jv} \le 0.05$, black marks $\xi_{jv} \ge 1.40$. The respective translational energies in the B state are shown with gray shading (light gray for $E_{\rm trans} \le 0.15$ eV; dark gray for $E_{\rm trans} \ge 2.00$ eV). (d) The Massey parameter $\xi_{\rm eff}(v)$ as a function of v calculated from the quantum distributions in (a) and (b) (filled histograms) using Eq. (23). The photon energy in panels (a–d) is $E = 5.49$ eV (the photolysis wavelength $\lambda = 226$ nm). (e) Experimental (red) and calculated (blue) photoemission spectrum of ozone photoexcited at 266 nm as function of the scattered photon wavelength λ_S. he experimental emission spectrum is redrawn from Fig. 1 of Ref. 42. The intensities of the first and the third calculated peaks are set equal to their experimental counterparts. Pure symmetric stretch excitations in $\tilde{X}$ are assigned.

numbers are weakly populated in the incident distribution and the reconstruction becomes less accurate. Extensions of the LZ model, which include non-diagonal matrix elements $j \to j'$ and $v \to v'$, are discussed in Sect. IV of ESI.†

The local Massey parameter $\xi_{jv}(X_\star)$ links the shape of the potentials near the conical intersection with the intermediate distributions in the local transverse modes. The dependence of $\xi_{jv}(X_\star)$ on the quantum numbers j and v, shown in Fig. 2(c) for $X_\star = 3.9\,a_0$, can be regarded as a two dimensional dynamical map of the intersection as seen by the separating fragments. Each (j,v) state is colored according to the value of the Massey parameter; the underlying gray shading shows the corresponding translational energy along X, $E_{\rm trans} = \mu_X \dot{X}_{jv}^2/2$; the fastest fragments are located near the origin $(j=0, v=0)$, and $E_{\rm trans}$ decreases as one moves towards the outer edge of the two dimensional map. As expected, $\xi_{jv}(X_\star)$ gradually increases with decreasing $E_{\rm trans}$ and with growing vibrational excitation: The dot color is generally darker at the outer edge than near the origin. However, the Massey parameter is influenced by the local stretch and bend differently. The impact of the short O−O bond quantum number is strong, and ξ_{jv}, as well as the transition probability $w_{jv}^{\rm LZ}(B \to R)$, quickly grow with v; as one moves along the v axis, the dot color noticeably darkens. The reason is the simultaneous growth of the coupling strength $\left(V_{AB}^2\right)_{jv}$ and the decrease of the velocity $\dot{X}_{jv}$. In contrast, $\xi_{jv}(X_\star)$ is only weakly dependent on the bending quantum number j, and the dot color barely changes along the j axis: The coupling strength is approximately independent of the seam coordinate Z and the Landau-Zener transition probability is mainly determined in the branching space rather than in the seam space. In the coordinate space (Y,Z), the energy difference between adiabatic states near conical intersection follows a similar pattern: It depends strongly on the coupling mode Y and is independent of the seam mode Z. Note that the influence of the gradient factor in the local Massey parameter on the transition probability appears to be far weaker than the influence of either the coupling or the velocity factors. This is further illustrated in Appendix A which shows that the coupling mode gradient of the lower adiabatic surface is insufficient to create an inverted vibrational distribution along the adiabatic path.

Extraction of Massey parameter is equivalent to mapping out the key topographic characteristics of a conical intersection, and this task can be accomplished using the Landau-Zener relation (22) between the incident, $P_B(j,v)$, and the transmitted, $P_R(v)$, distributions. Because ξ_{jv} is nearly independent of the seam quantum number j, the sum over j on the right-hand side of Eq. (22) can be evaluated, giving the incident distribution $P_B(v)$ in the O−O stretch shown in Fig. 2(a). The equation can now be inverted to give the effective Massey parameter in terms of the two intermediate distributions:

$$\xi_{\rm eff}(v) = -\ln\left(1 - \frac{P_R(v)}{P_B(v)}\right) \tag{23}$$

In Fig. 2(d), the approximate Massey parameter $\xi_{\rm eff}(v)$ is reconstructed from the quantum mechanical intermediate distributions in panels (a) and (b) as a function of v. The agreement with the v dependence of ξ_{jv} in panel (c) is fair for $v \le 15$; for larger v the B state population is very small and Eq. (23) becomes unreliable. Thus, an 'experiment' detecting intermediate vibrational distributions in the coupling mode Y is capable of delivering the effective Massey parameter for the nearby conical intersection.

5 Intermediate distributions from the Raman emission amplitudes

Emission spectroscopy[16,47] might be potentially applicable to detection of the intermediate distributions of interacting photofragments. The cross correlation function $C_{\gamma jv}(t|X_\star)$ in Eq. (19) can be represented as a full-space overlap integral,

$$C_{\gamma jv}(t|X_\star) = \langle \chi_{\gamma jv}(Y,Z|X_\star) g(X-X_\star) | \Phi_\gamma(t) \rangle\,, \tag{24}$$

of the wave packet $\Phi_\gamma(t)$, moving on the electronic surface γ, with the projection state $\chi_{\gamma jv}(Y,Z|X_\star)g(X-X_\star)$. Integration in angular brackets $\langle\cdot|\cdot\rangle$ is carried out over all three coordinates (X,Y,Z); $g(X-X_\star)$ is a function localized near $X_\star$. Strictly speaking, $g(X-X_\star)$ is a delta function $\delta(X-X_\star)$ [see Eq. (19)], but in practical calculations any function sufficiently localized around $X = X_\star$ will lead to a similar $C_{\gamma jv}(t|X_\star)$. Now the cross correlation function — and consequently the intermediate distributions — can be expressed in terms of the resonance Raman amplitudes[48]

$$\alpha_{k0}^\gamma(E_{\rm ph}) = \int_0^\infty \langle \phi_k | \Phi_\gamma(t) \rangle \exp(iE_{\rm ph}t)\, dt \tag{25}$$

for emission into the vibrational states ϕ_k of the ground electronic states $\tilde{X}$. This is achieved by expanding the localized projection state in terms of complete set of bound states ϕ_k,

$$\chi_{\gamma jv}(Y,Z|X_\star) g(X-X_\star) \approx \sum_k a_k^\gamma(X_\star)\phi_k(X,Y,Z) \tag{26}$$

With this expansion, the cross correlation function $C_{\gamma jv}(t|X_\star)$ in Eq. (24) and the T-matrix elements in Eq. (20) become linear combinations of α_{k0}^γ:

$$\begin{aligned}
\left|T_{\gamma jv}(E_{\rm ph}|X_\star)\right|^2 &= \frac{k_{\gamma jv}(X_\star)}{\mu_X}\left|\int_0^\infty C_{\gamma jv}(t|X_\star) e^{iE_{\rm ph}t} dt\right|^2 \\
&= \frac{k_{\gamma jv}(X_\star)}{\mu_X}\left|\sum_k \int_0^\infty \langle \chi_{\gamma jv} g|\phi_k\rangle\langle\phi_k|\Phi_\gamma(t)\rangle e^{iE_{\rm ph}t} dt\right|^2 \\
&= \frac{k_{\gamma jv}(X_\star)}{\mu_X}\left|\sum_k \left(a_k^\gamma(X_\star)\right)^* \alpha_{k0}^\gamma(E_{\rm ph})\right|^2 .
\end{aligned} \tag{27}$$

In order to elicit the accuracy of Eq. (27), a complete set $\{\phi_k\}$ of about 250 bound vibrational states in one potential well of the $\tilde{X}$ state is calculated. For these states, the complex Raman amplitudes α_{k0}^γ are evaluated for ozone dissociating in the coupled B and R states. Technical details of these calculations are summarized in Appendix B. The emission spectrum $\sigma_{\rm ram}(E_{\rm ph}, E_{\rm S}) \sim E_{\rm ph}E_{\rm S}^3 \sum_k \left|\alpha_{k0}^B + \alpha_{k0}^R\right|^2 \delta(E_{\rm S} - E_k)$, for the incident photon wavelength of 266 nm ($E_{\rm ph} = 4.66$ eV) is compared with the experimental spectrum of Ref. 42 in Fig. 2(e). The calculated spectrum stems mainly from the B state, agrees with experiment over a broad range of scattered photon wavelengths $\lambda_{\rm S}$, and quantita-

tively reproduces the rapidly decreasing intensity with growing λ_S, the multiplet structure of the emission, and the intensity patterns within multiplets. In particular, the enhanced emission intensity into pure symmetric stretch overtones in $\tilde{X}$ is excellently reproduced. This is the first calculated spectrum demonstrating a one-to-one comparison in the measured emission band intensities up to $\lambda_S = 320\,\text{nm}$ and it clearly points out the emission lines stemming directly from the molecule undergoing an ultrafast dissociation on the time scale of 200 fs. The basis set $\{\phi_k\}$ in $\tilde{X}$ is next used to represent the projection states and to calculate the expansion coefficients $a_k^\gamma(X_\star)$. The function $g(X-X_\star)$ in the projection states is chosen as a rectangle $X_\star - 0.1\,a_0 \le X \le X_\star + 0.1\,a_0$ localized at $X_\star = 3.9\,a_0$. Finally, the amplitudes α_{k0}^γ and the coefficients $a_k^\gamma(X_\star)$ are used in Eq. (27) to calculate the intermediate distributions.

The O−O vibrational distribution in the B state, reconstructed from the Raman amplitudes α_{k0}^B, is shown in Fig. 2(a) with empty histograms. The exact quantum mechanical distribution peaking at $v = 0$ is clearly well reproduced. The very long-v tail of the distribution is missing because most of the bound states $\{\phi_k\}$ capable of representing the corresponding projection states do not extend to large interfragment distances of $X_\star = 3.9\,a_0$.

Detection of emission from the R state and converting it into intermediate vibrational distributions along the electronically adiabatic path is required in order to locate the intersection along the tuning mode[16] and to characterize its shape. However, both the detection and the conversion steps are challenging. Indeed, the emission is strongly quenched, because the dipole moment of the $\tilde{X} \leftarrow R$ transition ($\sim 0.04\,\text{D}$) is much smaller than that for the B state, and $|\alpha_{k0}^R| \ll |\alpha_{k0}^B|$ (however, the polarization directions of the emitted photons in the two transitions are orthogonal, see Appendix B). Moreover, the R state is purely repulsive, and the corresponding molecular eigenstates are scattering states with vanishing amplitude at small interfragment distances. As a result, most of the R state emission is into the dissociation continuum of the $\tilde{X}$ state (the so-called *wing emission*[49]). The R state distributions can therefore be reliably calculated only from the continuum part of the emission spectrum. We illustrate this point by augmenting the bound basis $\{\phi_k\}$ with $\sim 10^5$ scattering states spanning a 2.5 eV wide energy range above the first dissociation threshold of $\tilde{X}$. Most of the emission from the R state falls into this energy interval. The quasi-continuum basis functions are constructed as products of the asymptotic fragment eigenstates and the X-dependent functions as described in Appendix B.

The O−O vibrational distribution in the R state, reconstructed using both bound and scattering states, is shown in Fig. 2(b) with a gray solid line. The reconstruction properly captures the overall shape of the exact quantum mechanical distribution and the extent of the O−O bond excitation. It is worth noting that the main effect of the scattering quasi-continuum on the reconstructed distribution in the B state in Fig. 2(a) is to slightly enhance the population in the high-v tail bringing it in a better agreement with the exact result.

6 Conclusions

In this paper, we investigate a reactive exit channel conical intersection in the UV photodissociation of ozone, in which the tuning mode X is aligned along the reaction coordinate. Two findings emerge from the exact quantum mechanical calculations combined with a Landau-Zener type analysis of the interacting photofragments:

1. *Intermediate vibrational distributions in the 'transverse' coupling mode Y allow one to reverse engineer the local Massey parameter and to delineate the key parameters of the intersection in the branching space.* The unique structural information about the shape of the conical intersection carried by the intermediate distributions is mapped out in the framework of a three-dimensional Landau-Zener model. For ozone, the intermediate distributions in the O−O vibration become strongly inverted as the molecule crosses the intersection adiabatically, and more than 1.0 eV of vibrational energy is transferred into the coupling mode.

2. *Intermediate distributions can be reconstructed from the emission spectra of the two intersecting states.* For ozone, the resonance Raman spectrum quantitatively agreeing with experiment has been calculated for the first time. A complete set of Raman amplitudes is then used to evaluate the O−O vibrational distributions near conical intersection. Reconstruction of intermediate distributions in the repulsive dark R state, populated via non-adiabatic transitions in the exit channel, requires the continuum wing emission to be taken into account.

Appendix A Product state distributions on a single adiabatic potential energy surface

In this Appendix, a single adiabatic state calculation for the photodissociation in the triplet dissociation channel is described. The final vibrational state distributions are calculated using the lower adiabatic potential

$$V_{\text{ad}}(X,Y,Z) = \frac{V_B + V_R}{2} - \sqrt{\left(\frac{V_B - V_R}{2}\right)^2 + V_{BR}^2}\,.$$

A cut through this potential along X is shown in Fig. 4 (thick blue and red lines). The simulation allows one to separate the impact of the topology of the lower adiabatic potential energy surface and the impact of the two state dynamics on the shape of the vibrational distributions in the triplet channel. The one-state calculation is performed using the same settings and the same initial state as those in the two-state calculation.

The final vibrational state distributions are calculated using Eq. (13) and the populations for $E_{\text{ph}} = 5.49$ eV are given in Fig. 3 (top-right panel). The corresponding populations in the two-state problem are shown in the top-left panel. As discussed in the main text, this distribution, created in the B→R transition, is vibrationally hot, peaking around $V \approx 10-13$. On the contrary, the distribution calculated using the lower adiabatic state has a

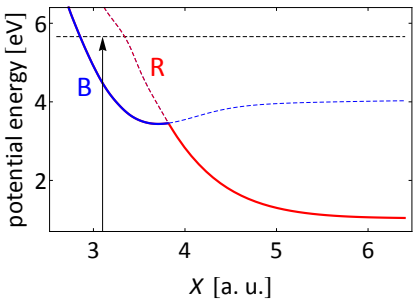

Fig. 4 Cut of the adiabatic potentials along the dissociation coordinate X. The coordinates (Y,Z) are fixed to the minimum of the diabatic B state. The lower adiabatic potential, used in the one-state calculation is marked with a thick line (blue for $X < X_{\rm CI}$, red for $X > X_{\rm CI}$). It is close to V_B (blue) at short distances and to V_R (red) at long distances. The dashed black line indicates the energy corresponding to the excitation with $\lambda = 226$ nm, for which the final vibrational distribution is shown in Fig. 3.

maximum at $V = 0$, and the population decreases quickly with increasing V, resembling the distribution on the B channel in the two-state problem.

Fixed energy components of the wave packets are shown in the lower panels of Fig. 3 for the one-state (right panel) and the two-state (left panel) calculations. They illustrate a dramatic change which the photodissociation dynamics in the R channel undergoes upon removing the upper electronic state. In particular, the large amplitude vibrations of the emerging molecular fragment are completely suppressed in the one-state calculation.

Appendix B Calculation of the Raman spectrum and reconstruction of the intermediate distributions

The resonance Raman amplitudes α^{γ}_{k0} (or: elements of the molecular polarizability tensor) for the emission from an electronic state γ into the vibrational states $\{\phi_k(\mathbf{Q})\}$ of the ground electronic states $\tilde{X}$ are given by half-Fourier transforms of the cross correlation functions of the evolving wave packet $\Phi_\gamma(t)$ with the functions ϕ_k via Eq. (25). The emission of a (scattered) photon with energy $E_{\rm S}$ follows the absorption from the vibrational ground state of $\tilde{X}$ at a fixed incident photon energy $E_{\rm ph}$; such emission spectrum was measured in the experiments of Kinsey and co-workers.[42] This spectrum is efficiently simulated using the stationary energy component $\mathbf{\Psi}^{\lambda}(\mathbf{Q}|E_{\rm ph})$ [Eq. (6)], which in the present context is often referred to as a Raman wave function. With $\mathbf{\Psi}^{\lambda}(\mathbf{Q}|E_{\rm ph})$, the emission amplitudes are given by the overlap[50]

$$\alpha^{\gamma}_{k0}(E_{\rm ph},E_{\rm S}) = \langle \phi_k | \Psi^{\lambda}_{\gamma}(E_{\rm ph}) \rangle \,. \qquad (28)$$

The ingredients leading to the emission amplitudes of Eq. (28) include (a) the function $\Psi^{\lambda}_{\gamma}(E_{\rm ph})$, (b) the basis states $\{\phi_k(\mathbf{Q})\}$, and (c) the transition dipole moments (TDMs) $\boldsymbol{\mu}_{B\tilde{X}}$ and $\boldsymbol{\mu}_{R\tilde{X}}$ between the $\tilde{X}$ state and the B and R states, respectively. Raman wavefunctions (see for example Fig. 3, bottom-left panel) are briefly discussed in the ESI.† The items (b) and (c) are discussed below.

Note that the emission spectrum $\sigma^{\gamma}_{\rm ram} \sim \sum_k |\alpha^{\gamma}_{k0}(E_{\rm ph},E_{\rm S})|^2 \delta(E_k - E_{\rm S})$ can be evaluated[50] as a Fourier transform of the autocorrelation function generated via a propagation of $\Psi^{\lambda}_{\gamma}(E_{\rm ph})$ in the ground electronic state $\tilde{X}$ with the Hamiltonian $\hat{H}_{\tilde{X}}$:

$$\sigma^{\gamma}_{\rm ram}(E_{\rm ph},E_{\rm S}) \sim E_{\rm ph}E_{\rm S}^3 \int_0^{\infty} \left\langle \Psi^{\lambda}_{\gamma} \left| e^{-i\hat{H}_{\tilde{X}}t} \right| \Psi^{\lambda}_{\gamma} \right\rangle e^{i(E_{\rm ph}-E_{\rm S})t} dt \,. \qquad (29)$$

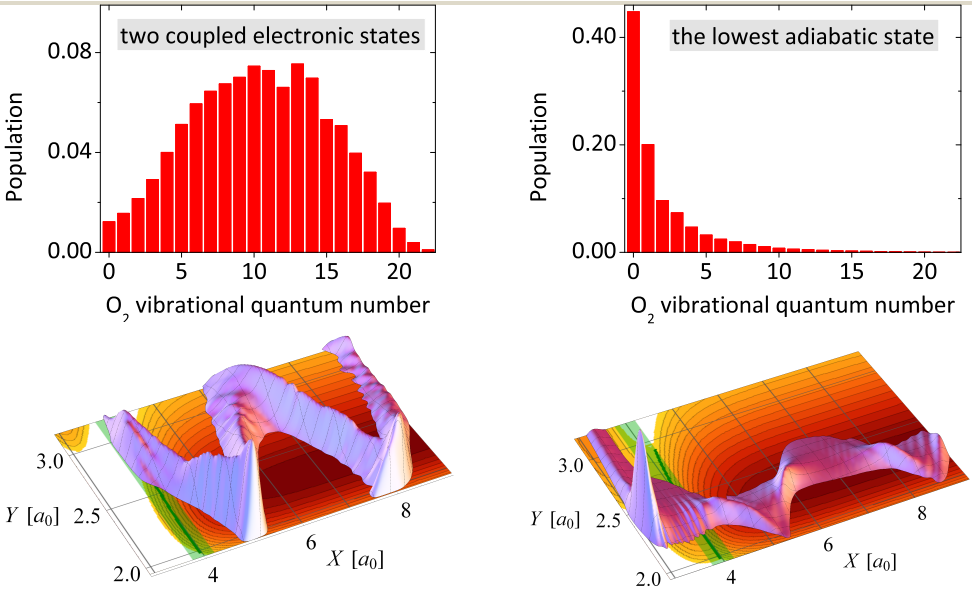

Fig. 3 Final vibrational state distributions for $E_{\rm ph} = 5.49$ eV: (left panel) in the R channel for the two-state system (full Hamiltonian); (right panel) arising from the dynamics on the lower adiabatic potential energy surface (single state Hamiltonian). The bottom panels show the squares of the energy components of the wave packets in the (X,Y)-plane, integrated over Z.

An explicit construction of the basis states $\{\phi_k\}$ can be avoided in this case.

B.1 Basis states in the ground electronic state

The vibrational basis states $\{\phi_k(\mathbf{Q})\}$ have been calculated using the potential energy surface of the ground electronic state as described in the ESI.† All calculated eigenstates were either symmetric or antisymmetric with respect to the interchange of the two end atoms. A total of 244 states (138 symmetric and 106 antisymmetric states) were found.

Transitions terminating on the bound states $\{\phi_k\}$ constitute the main part of the emission spectrum of ozone dissociating in the B state. In order to calculate the contribution to the emission spectrum from the R state, the set $\{\phi_k\}$ has to be augmented with the continuum basis states $\{\phi_n^-(E_S)\}$ lying above the ground-state dissociation threshold. Indeed, the R state is purely repulsive, and the corresponding molecular eigenstates, populated from the B state at relatively large interfragment distances near the conical intersection, are scattering states with vanishing amplitude at small interfragment distances. Under these circumstances, the *wing emission* into the dissociation continuum of the $\tilde{X}$ state is expected to be dominant. In many molecules, the wing emission corresponds to a broad featureless spectral region.[49] In ozone, emission into relatively narrow resonance states lying ca. 0.25 eV above the dissociation threshold has also been observed.[51]

In order to illustrate the shape of the wing emission from the R state, scattering basis states $\phi_n^-(E_S)$ in $\tilde{X}$ are constructed in Jacobi coordinates (X,Y,Z) in a given arrangement dissociation channel. For each scattered photon energy E_S (i.e., for each energy in the $\tilde{X}$ state $E_{\tilde{X}} = E_{ph} - E_S$), approximate basis states are constructed as products of X- and (Y,Z)-dependent functions. The (Y,Z)-dependent factor is a rovibrational state $\chi_n(Y,Z)$ of the $O_2(^3\Sigma_g^-)$ fragment with energy ε_n. The X-dependent factor is a scattering solution of a one-dimensional Schrödinger equation, with an effective vibrationally adiabatic potential, for the translational energy $E_{trans} = k_n^2/2\mu_X = E_{\tilde{X}} - \varepsilon_n$. Although this procedure produces distorted wave functions, it gives a large (and ideally a complete) set of both resonance and purely scattering basis states.[52] The energies E_S form an equidistant grid of 500 points in the energy interval $[2.0-5.0]$ eV; for each E_S, all open channels are included. This results in about 100 000 mutually orthogonal scattering basis states. The spectra shown below demonstrate that most of the emission from the R state falls into the chosen energy window.

B.2 Ab initio transition dipole moments

The TDM $|\boldsymbol{\mu}_{B\tilde{X}}|$ between B and $\tilde{X}$ is a spline interpolation of the ab initio data of Ref. 39. The TDM $\boldsymbol{\mu}_{R\tilde{X}}$ between R and $\tilde{X}$ has been calculated with an AVTZ basis set of Dunning at the CASSCF level of theory over a range of bond distances covering a broad vicinity of the conical intersection. It is shown in Fig. 5 as a function of one O−O bond length. In the spectral calculations, it is set to a constant value of $\mu_{R\tilde{X}} = 0.02$ a.u.

Near the conical intersection, the TDM $\mu_{B\tilde{X}}$ is close to 0.06 a.u. which is three times larger than $\mu_{R\tilde{X}}$, implying that the molecules staying in the B state and following the diabatic path through the

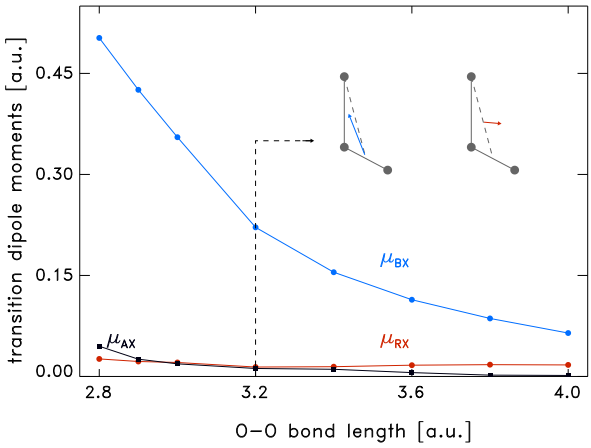

Fig. 5 Diabatic transition dipole moments of the three lowest singlet excited states with the ground electronic state $\tilde{X}$ shown as functions of one O−O bond distance. The other bond distance is fixed at $2.30\,a_0$ and the valence angle is fixed at 117°. The diabatic states are labelled B, R, and A. Two molecular diagrams illustrate the direction of the TDM vectors for the B state (blue) and the R state (red) for the bond distance of $3.2\,a_0$, close to the B/R conical intersection. The dashed line in the two diagrams is the Jacobi distance X, i.e. the dissociation coordinate.

intersection dominates the emission spectrum. At the same time, photons emitted from the two states have different polarizations. Indeed, although both B and R states are of A' symmetry and their TDM vectors lie in the molecular plane, the directions of the vectors $\boldsymbol{\mu}_{B\tilde{X}}$ and $\boldsymbol{\mu}_{R\tilde{X}}$ in this plane are different (see Fig. 5). For the B state, the vector $\boldsymbol{\mu}_{B\tilde{X}}$ is mainly aligned along the dissociation coordinate X. For the R state, the vector $\boldsymbol{\mu}_{R\tilde{X}}$ is essentially perpendicular to the dissociation direction. Thus, the emission along the diabatic path (B state) is parallel whereas the adiabatic path (R state) produces photons via a perpendicular TDM. The situation turns out to be similar to that encountered in the photodissociation of CH_3I.[16]

We note in passing that the photofragments heading into the diabatic and the adiabatic dissociation channels can also be distinguished by the anisotropy parameters[53] β of their intermediate angular distributions. A large positive β is expected for the $O\cdots O_2$ complexes moving diabatically in the B state, while a substantially reduced or even negative β is expected for fragments dissociating along the adiabatic path. These expectations are actually confirmed by the direct quantum mechanical calculations of rotating ozone.[15]

B.3 Raman spectra

The photoemission spectra of the B state, $\sigma_{ram}^B(E_{ph},E_S) \sim E_{ph}E_S^3\sum_k |\alpha_{k0}^B|^2\,\delta(E_S - E_k)$, for the excitation wavelengths $\lambda_I = 266$ nm and $\lambda_I = 226$ nm are shown in Figs. 2(e) and 6(a), respectively, as function of the scattered photon wavelength λ_S.

There is no published experimental spectrum at this wavelength; comparison with experiment is made for $\lambda_I = 266$ nm in Fig. 2. The overall structure of the emission is similar for these two excitation wavelengths. Characteristic are the quick decrease of the emission intensity with growing λ_S, as the progressively more excited vibrational states of the ground-state ozone are

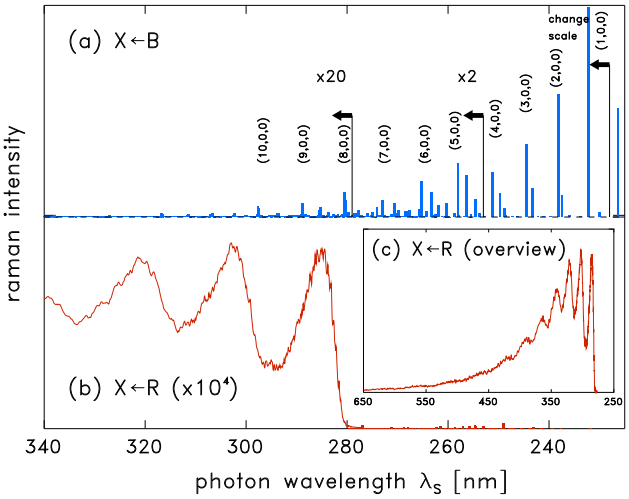

Fig. 6 The calculated photoemission spectrum of ozone photoexcited at 226 nm as function of the scattered photon wavelength λ_S. (a) Emission from the B state. The intensities of the first and the third calculated peaks are scaled as in Fig. 2 of the main article. The wavelength at which the intensities are multiplied by a factor of 20 marks the position of dissociation threshold in $\tilde{X}$ ($\lambda_S \geq 280\,\text{nm}$). Pure symmetric stretch excitations are assigned below and above dissociation threshold. (b) Emission from the R state. The emission intensity is 10^4 times weaker than that from the B state. Panel (c) shows the R state emission over a much broader wavelength interval of $230\,\text{nm} \leq \lambda_S \leq 650\,\text{nm}$.

reached, and the polyad structure of the emission spectrum, with the intensity noticeably enhanced for the pure symmetric stretch excitations in $\tilde{X}$. The contribution of wing emission, observed above the dissociation threshold of the $\tilde{X}$ state for $\lambda_S \geq 280\,\text{nm}$, is small for the B state. However, a progression of narrow resonance states can be clearly isolated in the calculated emission spectrum for $\lambda_S \geq 280\,\text{nm}$. Their wave functions correspond to pure symmetric stretch excitations and are assigned $(8,0,0)$, $(9,0,0)$, and $(10,0,0)$ in Fig. 6(a). A quantitatively similar above-threshold emission progression has been detected in Ref. 51 for $\lambda_I = 266\,\text{nm}$.

The photoemission spectrum for the R state, $\sigma^R_{\text{ram}}(E_{\text{ph}}, E_S) \sim E_{\text{ph}} E_S^3 \sum_k |\alpha^R_{k0}|^2 \delta(E_S - E_k)$, is shown in panel (b). Two features distinguish it from the emission from the B state. First, the R-state emission is about 10^4 times weaker than the B-state emission. This is partly because of difference in the TDMs for the two states and partly because the R state is populated only via non-adiabatic transitions from the B state; the non-adiabatic transition probability lies below 10% at this E_{ph}. Second, the dependence of the R-state emission intensity on λ_S is very different from that observed for the B state and has a pronounced threshold. There is essentially no emission into the bound states, and the intensity abruptly rises by about two orders of magnitude as the dissociation threshold of $\tilde{X}$ is crossed. The emission maximum is reached approximately 0.5 eV above threshold, but a structured emission tale extends far into the visible range up to $\lambda_S \approx 600\,\text{nm}$ (see panel (c) of Fig. 6). The present calculations predict that the long wavelength limit of the emission spectrum of ozone is dominated by the R state emission.

Acknowledgements

Financial support by the Deutsche Forschungsgemeinschaft is gratefully acknowledged. The authors would like to thank P. Houston for advice and a careful reading of the manuscript, W. Domcke for numerous discussions of the dynamics at conical intersections, and A.R. Ravishankara for a thought provoking discussion on the emission spectrum of the photodissociating ozone.

References

1 W. Domcke, D. R. Yarkony and H. Köppel, Eds., *Conical Intersections*, World Scientific, Singapore, 2012.
2 B. G. Levine and T. J. Martinez, *Annu. Rev. Phys. Chem.*, 2007, **58**, 613.
3 N. J. Turro, V. Ramamurthy and V. C. Scaiano, *Principles of Molecular Photochemistry: An Introduction*, University Science Books, USA, 2000.
4 H. J. Worner, J. B. Bertrand, B. Fabre, J. Higuet, H. Ruf, A. Dubrouil, S. Patchkovskii, M. Spanner, Y. Mairesse, V. Blanchet, E. Mevel, E. Constant, P. B. Corkum and D. M. Villeneuve, *Science*, 2011, **334**, 208.
5 J. Krčmář, M. F. Gelin, D. Egorova and W. Domcke, *J. Phys. B: At. Mol. Opt. Phys.*, 2014, **47**, 124019.
6 D. Polli, P. Altoe, O. Weingart, K. M. Spillane, C. Manzoni, D. Brida, G. Tomasello, G. Orlandi, P. Kukura, R. A. Mathies, M. Garavelli and G. Cerullo, *Nature*, 2010, **467**, 440.
7 J. S. Lim and S. K. Kim, *Nature Chemistry*, 2010, **2**, 627.
8 The impact of motion in the seam space on the rate of a non-adiabatic reaction is dicussed in the review by M. Robb in Ref. 1 (p. 3), where several examples of the reaction coordinate running parallel to the intersection seam are considered..
9 M. N. R. Ashfold, G. A. King, D. Murdock, M. G. D. Nix, T. A. A. Oliver and A. G. Sage, *Phys. Chem. Chem. Phys.*, 2010, **12**, 1218.
10 M. L. Hause, Y. H. Yoon, A. S. Case and F. F. Crim, *J. Chem. Phys.*, 2008, **128**, 104307.
11 M. N. Daud, G. G. Balint-Kurti and A. Brown, *J. Chem. Phys.*, 2005, **122**, 054305.
12 S. Y. Grebenshchikov, *J. Chem. Phys.*, 2013, **138**, 224106.
13 S. Y. Grebenshchikov, *J. Chem. Phys.*, 2013, **138**, 224107.
14 S. Y. Grebenshchikov, Z.-W. Qu, H. Zhu and R. Schinke, *Phys. Chem. Chem. Phys.*, 2007, **9**, 2044.
15 D. Picconi and S. Y. Grebenshchikov, *J. Chem. Phys.*, 2014, **141**, 074311.
16 K. Q. Lao, M. D. Person, P. Xayariboun and L. J. Butler, *J. Chem. Phys.*, 1990, **92**, 823.
17 Y.-J. Jung, M. S. Park, Y. S. Kim, K.-H. Jung and H.-R. Volpp, *J. Chem. Phys.*, 1999, **111**, 4005.
18 R. de Nalda, J. Durá, A. García-Vela, J. G. Izquierdo, J. González-Vázquez and L. B. nares, *J. Chem. Phys.*, 2008, **128**, 244309.
19 C. R. Evenhuis and U. Manthe, *J. Phys. Chem. A*, 2011, **115**, 5992.
20 A. L. Sobolewski, W. Domcke, C. Dedonder-Lardeux and C. Jouvet, *Phys. Chem. Chem. Phys.*, 2002, **4**, 1093.

21 A. S. Chatterley, J. D. Young, D. Townsend, J. M. Zurek, M. J. Paterson, G. M. Roberts and V. G. Stavros, *Phys. Chem. Chem. Phys.*, 2013, **15**, 6879.

22 L. D. Landau and E. M. Lifshitz, *Quantum Mechanics. Nonrelativistic Theory*, Pergamon, New York, 1976.

23 Z.-W. Qu, H. Zhu, S. Y. Grebenshchikov and R. Schinke, *J. Chem. Phys.*, 2005, **122**, 191102.

24 E. Teller, *J. Phys. Chem.*, 1937, **41**, 109.

25 A. L. Devine, M. G. D. Nix, R. N. Dixon and M. N. R. Ashfold, *J. Phys. Chem. A*, 2008, **112**, 9563.

26 Y.-T. W. S. Yan and K. Liu, *Proc. Nat. Acad. Sci.*, 2008, **105**, 12667.

27 A. R. Ravishankara, G. Hancock, M. Kawasaki and Y. Matsumi, *Science*, 1998, **280**, 60.

28 P. J. Hay, R. T. Pack, R. B. Walker and E. J. Heller, *J. Phys. Chem.*, 1982, **86**, 862.

29 Y. Matsumi and M. Kawasaki, *Chem. Rev.*, 2003, **103**, 4767.

30 S. Y. Grebenshchikov and S. Rosenwaks, *J. Phys. Chem. A*, 2010, **114**, 9809.

31 R. Schinke and G. C. McBane, *J. Chem. Phys.*, 2010, **132**, 044305.

32 B. R. Johnson, B. Chang, C. Hsiao, L. Le and J. L. Kinsey, *J. Chem. Phys.*, 1998, **108**, 7670.

33 H. Köppel, in *Conical Intersections*, ed. W. Domcke, D. R. Yarkony and H. Köppel, World Scientific, Singapore, 2004.

34 J. Zhang, *Theory and Application of Quantum Molecular Dynamics*, World Scientific, Singapore, 1999.

35 G. G. Balint-Kurti, R. N. Dixon and C. C. Marston, *J. Chem. Soc. Faraday Trans.*, 1990, **86**, 1741.

36 G. G. Balint-Kurti, *Adv. Chem. Phys.*, 2004, **128**, 249.

37 D. E. Manolopoulos and M. H. Alexander, *J. Chem. Phys.*, 1992, **97**, 2527.

38 M. H. Alexander, C. Rist and D. E. Manolopoulos, *J. Chem. Phys.*, 1992, **97**, 4836.

39 E. Baloïtcha and G. G. Balint-Kurti, *J. Chem. Phys.*, 2005, **123**, 014306.

40 S. M. Dylewski, J. D. Geiser and P. L. Houston, *J. Chem. Phys.*, 2001, **115**, 7460.

41 H. Köppel, W. Domcke and L. S. Cederbaum, *Adv. Chem. Phys.*, 1984, **57**, 59.

42 D. G. Imre, J. L. Kinsey, R. W. Field and D. H. Katayama, *J. Phys. Chem.*, 1982, **86**, 2564.

43 X.-P. Zhang, W.-B. Lee and K.-C. Lin, *J. Phys. Chem. A*, 2009, **113**, 35.

44 J. Malhado and J. Hynes, *Chem. Phys.*, 1995, **347**, 39.

45 A. Piryatinsky, M. Stepanov, S. Tretiak and V. Chernyak, *Phys. Rev. Lett.*, 2005, **95**, 223001.

46 R. R. Dogonadze and Z. D. Urushadze, *J. Electroanal. Chem.*, 1971, **32**, 235.

47 B. R. Johnson, C. Kittrell, P. B. Kelly and J. L. Kinsey, *J. Phys. Chem.*, 1996, **100**, 7743.

48 S. Y. Lee and E. J. Heller, *J. Chem. Phys.*, 1979, **71**, 4777.

49 D. G. Imre, J. L. Kinsey, A. Sinha and J. Krenos, *J. Phys. Chem.*, 1984, **88**, 3956.

50 E. J. Heller, R. L. Sundberg and D. Tannor, *J. Phys. Chem.*, 1982, **86**, 1822.

51 B.-Y. Chang, C.-Y. Kung, C. Kittrell, C.-W. Hsiao, B. R. Johnson, S. G. Glogover and J. L. Kinsey, *J. Chem. Phys.*, 1994, **101**, 1914.

52 M. Ivanov, S. Y. Grebenshchikov and R. Schinke, *J. Chem. Phys.*, 2004, **120**, 10015.

53 R. N. Zare, *Angular Momentum*, Wiley, New York, 1988.